Angular dependence of static and kinetic friction on alkali halide surfaces

Pascal Steiner,* Raphael Roth,† Enrico Gnecco,‡ Alexis Baratoff, and Ernst Meyer
Department of Physics, University of Basel, Klingelbergstr. 82, 4056 Basel, Switzerland
(Received 12 April 2010; revised manuscript received 27 September 2010; published 10 November 2010)

The angular dependence of the lateral forces acting on an atomically sharp tip slowly pulled by an elastic spring along a crystal surface with square symmetry is investigated in the framework of a separable two-dimensional tip-surface interaction potential. In the stick-slip regime kinetic friction is proportional to $(\cos\varphi+|\sin\varphi|)$, φ being the angle between the scan direction and a particular symmetry axis. For a high enough normal force, static friction is proportional to $1/\cos\varphi$, whereas for intermediate loads it shows a φ-dependent spread of possible values. Continuous sliding with ultralow friction sets in below a load-dependent corrugation amplitude. Numerical simulations help interpret those analytic results in terms of the zigzag motion of a friction force microscope tip sliding on the (001) surface of a rocksalt crystal. The influence of the offset between the start of a scan and the center of the corresponding unit cell, in particular, for scans along ⟨100⟩ directions is also elucidated. The predicted ratio of kinetic friction along the ⟨100⟩ and ⟨110⟩ directions agrees best with values measured on alkali halides with similar cation and anion radii. This ratio, as well as the angular dependence of the static friction may be used to determine fine details of the lateral tip-sample interaction.

DOI: 10.1103/PhysRevB.82.205417 PACS number(s): 68.35.Af, 68.37.Ps, 07.79.Sp, 61.50.Ah

I. INTRODUCTION

A dependence of friction on the sliding direction (*friction anisotropy*) has been experimentally established even on high-symmetry crystal surfaces. In a pioneering study with a scratch apparatus, Bowden and co-workers reported a significantly higher friction along ⟨100⟩ directions on diamond, MgO, and LiF compared to ⟨110⟩ directions, which was attributed to enhanced surface damage along the former high-symmetry directions.[1] A similar trend was observed more recently by friction force microscopy (FFM) on the (001) cleavage surface of several alkali halide crystals and attributed to the enhanced corrugation of the tip-surface interaction potential along ⟨100⟩ directions.[2,3] A sinusoidal dependence of friction on the sliding angle was revealed in early investigations on diamond.[4] On the hexagonal cleavage plane of highly oriented pyrolitic graphite (HOPG), a remarkable suppression of friction (often called superlubricity) sometimes observed if the sample was rotated away from directions differing by 60° was attributed to the sliding of a graphite flake attached to the probing tip and incommensurately oriented with respect to the sample.[5] It is important to distinguish such effects which depend on this *misfit angle* from the dependence on the sliding or scan angle φ with respect to a particular high-symmetry axis on the sample surface. Special anisotropy effects reported on less symmetric samples with specific preferred directions are not considered here.

Only a few theoretical simulations, mostly based on the two-dimensional Prandtl-Tomlinson (2D-PT) model[6,7] or the Frenkel-Kontorova-Tomlinson (2D-FKT) model recently reviewed by Braun,[8] have dealt with friction, in particular, off-symmetry directions[9,10] or with friction anisotropy.[11,12] In the former model the tip is represented by a single particle, whereas in the latter a flake picked up by the tip, or the sliding counterpiece, is represented by a periodic array of particles connected by lateral springs. In both models the particle(s) interact with a 2D sinusoidal potential representing the sample surface and are connected by separate spring(s) to a support which is scanned at a constant velocity **v** parallel to the surface. The PT model is recovered in the absence of the lateral springs or in the limit of hard ones for matching sample and flake lattices (zero misfit). Broad maxima of the average lateral force in the scan direction (*kinetic friction*) around angles corresponding to ⟨100⟩ directions on (001) cleavage surfaces of rocksalt-type crystals and cusplike minima along ⟨110⟩ directions were found in the latter limit for square lattices.[11] For the force required to initiate sliding (*static friction*), however, cusplike maxima and broad minima were found along the above-mentioned directions in an equivalent 2D-FK model (zero misfit, lateral force directly applied to the support).[13] For finite misfit angles, friction, both kinetic and static, becomes much lower, as expected from canceling contributions from particles trapped at various positions in different minima of the corrugation potential, especially for misfits approaching incommensurability.[11] A similar behavior of the computed kinetic friction between a rigid flake and a corrugated surface potential, both having the graphene structure, was obtained by Verhoeven *et al.*,[12] except that the sharp maxima around zero misfit angles differing by 60° had a angular finite width equal to the flake diameter in units of the lattice constant. For zero misfit they found a dependence of the kinetic friction on scan angle with broad maxima along directions of maximum corrugation and with sharper minima along symmetry directions halfway in between. They could thus interpret the experimental results from the same group on HOPG.[5,14]

These pioneering experiments were conducted with a complex dedicated instrument designed to independently detect force components acting on the tip in three orthogonal directions. In conventional FFM setups, however, only the torsional and flexural deflections of the cantilever with a tip at its end are monitored. Whereas torsion is caused by the lateral force component perpendicular to the cantilever axis, flexure is due to the component perpendicular to the scanned surface, as well as to the bending moment exerted by the

lateral component parallel to the cantilever axis.[15] This third component typically dominates the flexural deflection in FFM measurements on atomically flat surfaces for applied normal loads of tens of nanonewtons, and thus distorts the "apparent topography."[16] Such observations motivated Fujisawa and co-workers[17,18] to reconstruct the 2D trajectory of the tip apex from lattice-resolved FFM measurements of both deflections.

Our goal, however, is to understand the 2D motion of a sharp tip as a function of scan angle at normal forces in the nanonewton range, by focusing on the (001) surface of alkali halide crystals where atomic-scale contacts can be realized.[19,20] Results can then be quantitatively compared to computations based on the PT model assuming zero misfit, without[19] or with[21,22] thermal effects included. Because the interpretation of the flexural signal becomes ambiguous at low normal forces, the dependence of friction on scan angle is most reliably studied via the torsional deflection while scanning perpendicular to the cantilever axis and incorporating a rotatable sample holder in a conventional FFM setup. Having such measurements in mind, we derive here analytical formulas describing the angular dependence of static and kinetic friction in the case of an atomically sharp tip slowly pulled by an elastic spring across a surface lattice with square symmetry whose corrugation is represented by its lowest 2D Fourier component.

The predicted dependencies exhibit the above-mentioned features computed using 2D-FKT models for zero misfit[11,13] and are interpreted in terms of the 2D motion of the tip apex, as revealed by our own numerical simulations. In particular, the origin of the cusps at the maxima of the static friction and the minima of the kinetic friction is clarified. Moreover, the *offset* between the first scan line and the potential minimum in the unit cell where it is started is shown to cause a spread of possible static friction values, although it has no effect on the kinetic friction. We also reexamine the determination of the corrugation amplitude which was introduced earlier on the basis of a comparison of lateral force profiles with one-dimensional (1D) simulations.[19] The predicted $\langle 100\rangle/\langle 110\rangle$ ratio agrees well with those measured on the (001) surface of alkali halides with similar cation and anion radii.[2,3] Finally we propose that the present model might provide a useful benchmark to detect deviations in friction anisotropy due to hitherto neglected higher components of the lateral tip-sample interaction potential.

II. MODEL

As in previous simulations of FFM on alkali halide (001) surfaces, which considered scans in high-symmetry directions,[23–25] the motion of the sharp FFM tip is described within the 2D-PT model. The system is represented by a point mass m elastically coupled to a rigid support by a spring of stiffness k. Comparisons between dry friction experiments in ultrahigh vacuum and numerical simulations on alkali halide surfaces have shown that for normal forces in the wearless nanonewton range, the spring constant k is dominated by the lateral stiffness of the contact region rather than by the torsion of the cantilever[19,20] and is essentially isotropic.[21] Furthermore, the nearly constant and low value of $k \sim 1-2$ N/m indicated that the contact is of atomic size. The elastic potential experienced by the FFM tip is expressed as

$$V_{\mathrm{el}}(x,y;t) = \frac{k}{2}[(x - x_0 - v_x t)^2 + (y - y_0 - v_y t)^2], \qquad (1)$$

where (x,y) are the coordinates of the tip apex, (x_0,y_0) those of the support at time $t=0$, and (v_x,v_y) the components of the scan velocity along the x and y axes. The scan direction is defined by the polar angle $\varphi = \arctan(v_y/v_x)$. The total potential experienced by the tip apex,

$$V_{\mathrm{tot}}(x,y;t) = V_{\mathrm{int}}(x,y) + V_{\mathrm{el}}(x,y;t), \qquad (2)$$

involves in addition the tip-sample interaction potential V_{int} which, for simplicity, is limited to its first 2D Fourier component compatible with square symmetry

$$V_{\mathrm{int}}(x,y) = -\frac{E_0}{2}\left(\cos\frac{2\pi x}{a} + \cos\frac{2\pi y}{a}\right). \qquad (3)$$

The total potential is then separable, i.e., x and y become decoupled. The quantity E_0 is the load-dependent corrugation of the tip-surface potential. The strength of the interaction energy V_{int} relative to the elastic energy V_{el} stored in the spring is quantified by the parameter $\eta = 2\pi^2 E_0/ka^2$. This parameter was used in previous 1D treatments to define the transition from atomic stick-slip ($\eta > 1$) to a superlubric ($\eta < 1$) regime of motion.[19,26] In view of the lattice periodicity, the offset (x_0,y_0) can be chosen to lie within the unit cell in which the first scan line is started. Indeed, in a real FFM experiment the corrugation of V_{int} switches on as the tip first comes into contact with the sample at a preset (x_0,y_0) support position.

Neglecting thermal effects, the tip motion is described by Newton's equation

$$m\frac{d^2\mathbf{r}}{dt^2} + m\Gamma\frac{d\mathbf{r}}{dt} + \nabla V_{\mathrm{tot}} = 0, \qquad (4)$$

where $\mathbf{r} \equiv (x,y)$ and Γ is the damping rate. Since alkali halides have been extensively studied by FFM,[2,3,19,20] we have chosen the (001) surface of rocksalt as a model system for testing our predictions. The unit cell of NaCl contains two different ionic species, but only a pattern showing the lattice periodicity is usually imaged in FFM. Note that the [100] and [010] directions are rotated by $\mp 45°$ with respect to our x and y axes and that the usual lattice constant ($a_1 = 0.564$ nm) corresponds $\sqrt{2}a$ in our notation. For comparison with our analytic results valid in the limit of vanishing temperature T and scan velocity, numerical simulations were performed using the velocity Verlet algorithm[27] adapted to include the damping term in Eq. (4) using a time step $\Delta t = 10^{-7}$ s and the parameters: $k=2$ N/m, $v=25$ nm/s, $\Gamma = 2.8\times 10^6$ s^{-1}, and $m = 10^{-12}$ kg.[21] This choice enables efficient computations on a PC while allowing an adequate sampling of the fast tip motion during slips. Moreover, the damping is close to critical damping, which ensures that all slips occur between adjacent unit cells.[21] Most numerical results illustrated here refer to $E_0 = 0.5$ eV; the parameter η is then

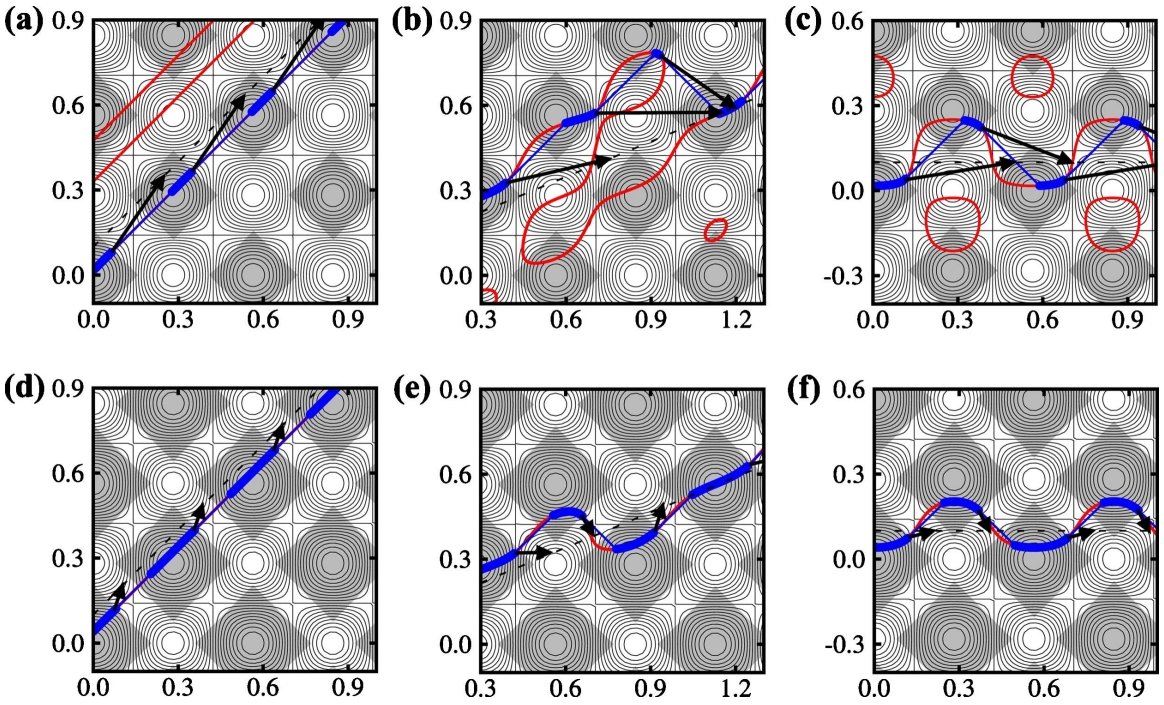

FIG. 1. (Color online) 1.0×1.0 nm^2 contour plots of the tip-surface interaction V_{int} on NaCl(001). The dashed lines indicate the scan line (support path), assuming an initial vertical offset of 0.1 nm from the minimum at the origin. The shaded areas denote the stability domains of the tip motion. Inside those areas the computed tip trajectories (thick blue points) essentially coincide with the loci where forces balance in the quasistatic limit (continuous red curve). Thin blue lines connect the initial and final tip positions in the course of slips between adjacent domains, whereas black arrows point toward the corresponding support positions. Scan lines and trajectories are shown for [(a)–(c)] $\eta=5$ and [(d)–(f)] $\eta=1.5$, for $\varphi=0°$ (left), which corresponds to the [110] direction, $\varphi=-22.5°$ (center) and $\varphi=-45°$ (right), which corresponds to the [100] direction.

close to 5, in accordance with FFM measurements with well-developed stick-slip friction without wear on NaCl(001).[19] A few Langevin simulations were also performed at room temperature in order to complement our previous study of 2D effects[21] which was restricted to scans parallel to [100].

III. RESULTS

A. Numerical simulations

Figure 1 illustrates portions of computed tip trajectories corresponding to three scan directions for [(a)–(c)] $\eta=5$ and [(d)–(f)] $\eta=1.5$, and a given finite initial offset. Starting from the corresponding equilibrium position in the closest-lying minimum of the interaction potential V_{int}, the tip slowly moves along a continuous trajectory until it reaches the boundary of the surrounding stability domain, then suddenly slips into an adjacent minimum. The lateral force $\mathbf{F}_c$ exerted by the spring just before a particular slip is proportional to the corresponding vector depicted as a black arrow in Fig. 1. While slipping, the tip avoids the maxima of the potential V_{int}. This leads to a distinct zigzag trajectory, except along $\langle 110 \rangle$ directions, as shown in Fig. 1(a). This zigzag behavior, which is characteristic of 2D friction, was first inferred by Fujisawa *et al.*[17] from lattice-resolved FFM measurements, most of which were performed along [100] and [010] directions[18] on the basal plane of hexagonal crystals (mica, graphite, MoS_2). The simple model which they proposed (tip *stick points* at the centers of adjacent unit cells) appeared to explain their results, but later the same group recognized that the 2D-PT model[23,28] provided a better description of their observations.[29] In our simulations, as a consequence of the separability of $V_{\text{tot}}(x,y;t)$, the tip trajectory is straight in $\langle 110 \rangle$ directions, but coincides with the scan line only if the offset y_0 vanishes. For arbitrary scan directions φ between $\pm 45°$, as shown in Fig. 1(b), successive slips along x are interrupted by y slips toward the support path once a certain transverse force is reached. For higher η, y slips merely succeed in maintaining the tip trajectory at a certain average distance from the scan line. This deviation changes sign when the scan direction is reversed. Indeed, between slips during the backward scan, the tip sticks on segments of the quasistatic equilibrium part of the red curve on the other side of the scan line. This causes a hysteresis loop in space, besides the well-known hysteresis in the lateral force, which leads to energy dissipation, i.e., net average friction. Note that the back-bending parts of the red curve lie outside stability domains and are therefore inaccessible. For scans parallel to a symmetry direction, no back bends occur, and backward scan tip trajectories are mirror images of forward ones with respect to the perpendicular symmetry axis. For scans along $\langle 100 \rangle$ directions, as illustrated in Fig. 1(c), and noticed by others,[18,23,24] each x slip is followed by a y slip of the same magnitude. For smaller values of $\eta > 1$, the overall behavior is similar, but the stability domains are larger, so that the slips become shorter, as illustrated in Figs. 1(d)–1(f),

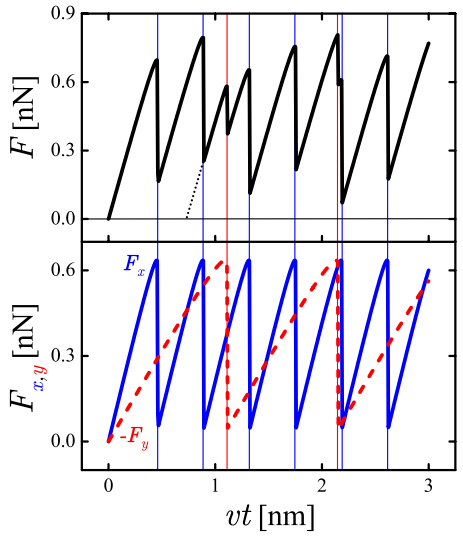

FIG. 2. (Color online) Top: computed dependence of the lateral force exerted by the spring for $\eta=5$ projected on the scan direction for $\varphi=-22.5°$ starting at $x_0=y_0=0$. Bottom: corresponding force components versus support displacement (for the chosen direction F_y is negative so that F_y is plotted together with F_x). Because the assumed interaction potential is separable, both components exhibit periodic stick-slip patterns only differing by horizontal stretches proportional to the velocity components v_x, v_y.

and the tip trajectory deviates less from the scan line.

The force measured in conventional FFM is given by the projection of the force $\mathbf{F}=(F_x,F_y)$ along the scan direction,

$$F_{\text{scan}} = F_x \cos\varphi + F_y \sin\varphi. \tag{5}$$

This quantity is plotted in the top half of Fig. 2 for a scan oriented as in Fig. 1(b) but with zero initial offset, i.e., starting from a potential minimum. The profile of F_{scan} is aperiodic, but the individual components $F_{x,y}$ exhibit similar sawtooth patterns with periods av_x/v, av_y/v, respectively. Each jump in F_{scan} coincides with a jump in F_x or F_y at the location of the support where an x or y slip occurs. The long-time averages $\langle F_x\rangle$ and $|\langle F_y\rangle|$ are therefore equal and the angular dependence of $\langle F_{\text{scan}}\rangle$ (the *kinetic friction* defined as the average friction force along the scan direction) solely arises from the explicit φ dependence in Eq. (5). The critical value of F_{scan} corresponding to the position of the *first slip* defines the *static friction* F_{stat} for a particular initial offset. For the assumed $\eta=5$, this value is slightly below the first maximum of F_{scan} but, as shown below, the deviation becomes appreciable if $\eta\to 1$.

For scans between $\langle 110\rangle$ and $\langle 100\rangle$ directions, the values of F_{scan} at the positions of the following slips define static friction values for different offsets, as can be seen in Fig. 1(e). Indeed, points on scan line segments within successively traversed unit cells may be considered as possible offsets for scans started there. However, as seen in Fig. 1(b), already for $\eta=5$ the tip can stick in side minima centered in unit cells which are not traversed by the scan line. According to our physically motivated definition of possible offsets, such metastable locations cannot be considered as commonly realized starting tip positions. A unique offset in each traversed cell can nevertheless be specified as the location where $F_{\text{scan}}=0$. Such locations along the scan line can be found by extrapolating each preceding stick segment down to 0 as approximately indicated by the dotted straight line in Fig. 2. For a general scan direction $v_y/v_x=\tan\varphi$ is an irrational number, and all possible offset values are therefore sampled along an infinitely long scan line. In the simulations, a sufficiently dense discrete sampling is achieved by scanning over several hundred unit cells. For scan angles approaching $\langle 110\rangle$ or $\langle 100\rangle$ directions, parallel to which the tip trajectories and force variations become periodic, such a dense sampling would require extremely long scans, however.

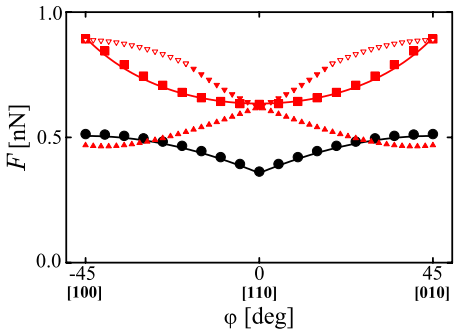

FIG. 3. (Color online) Angular dependence of the kinetic friction force $\langle F\rangle$ (black dots) and of the static friction force F_{stat} (red rectangles) for a scan starting at a minimum of the potential V_{int} corresponding to FFM measurements on NaCl(001) for $\eta=5$. The points obtained from simulations are in good agreement with analytic expression plotted as continuous lines. For finite initial offset, F_{stat} ranges between the red triangles pointing up and down which correspond to calculated minimum and maximum values.

The preceding discussion implies that $\langle F_{\text{scan}}\rangle$ *is independent of any initial offset, whereas* F_{stat} is not, hence covers a finite range, except for scans along $\langle 110\rangle$ for which $F_{\text{scan}}=F_x$, as illustrated in Fig. 3. Together with the analytic expressions derived below these conclusions constitute the two main results of our work.

B. Quasistatic limit

The curves describing the tip trajectories (Fig. 1) and the angle dependence of kinetic and static friction (Fig. 3) can be analytically determined. If the scan velocity is sufficiently small (*quasistatic limit*) the tip stays in a slowly evolving local minimum of the potential V_{tot} during each stick stage but rapidly slips to an adjacent minimum whenever the local equilibrium becomes marginally stable.[6,7]

For the assumed separable potential, the necessary condition for a minimum, $\nabla V_{\text{tot}}=0$ as a function of the support displacement $\mathbf{v}t$ leads to decoupled equations for x and y components, namely,

$$F_x = x_0 + v_x t - x = \eta \sin x,$$

$$F_y = y_0 + v_y t - y = \eta \sin y. \tag{6}$$

In Eq. (6) and the following ones we adopt reduced units such that every length must be multiplied by $a/(2\pi)$ and

every force by $ka/(2\pi)$. Eliminating t one obtains an analytical expression for the locus of points where the elastic and interaction forces balance, i.e.,

$$\frac{y - y_0 + \eta \sin y}{x - x_0 + \eta \sin x} = \frac{v_y}{v_x} \equiv \tan \varphi, \tag{7}$$

which generalizes to arbitrary offsets the expression used earlier.[21] Those loci are plotted as continuous red curves in Fig. 1, whereby only the branch lying near the support path is accessible if the tip dynamics is overdamped or critically damped, as assumed here. The tip equilibrium is stable if the conditions $\lambda_{1,2} > 0$ are satisfied, $\lambda_{1,2}$ being the eigenvalues of the Hessian matrix $\mathcal{H} = \partial^2 V_{\text{tot}} / \partial x_i \partial x_j$, as first emphasized by Gyalog *et al.*[9] For our separable potential the stability domains form an infinite array of square areas defined by the relations $\cos x > -1/\eta$ and $\cos y > -1/\eta$. These areas surround minima of the potential $V_{\text{int}}(x,y)$, but merge together and cover the entire x-y plane when $\eta \leq 1$. When this *transition to superlubricity* occurs, the above-mentioned locus no longer exhibits back bends and coincides with a unique and reversible tip trajectory which wiggles slightly around the scan line, as suggested by the apparent changes between Figs. 1(a)–1(f).

Taking the time derivative of Eq. (6), one notices that in the quasistatic approximation the tip velocity is given by

$$\dot{x} = v_x/(1 + \eta \cos x),$$

$$\dot{y} = v_y/(1 + \eta \cos y) \tag{8}$$

so that its x component appears to diverge when x reaches the stability boundary $x_c = \arccos(-1/\eta)$, and similarly for y. The quasistatic hypothesis must therefore break down before either boundary is reached. Numerical and analytical computations in the 1D case have shown that at low scan speed $\mathbf{v}$ the tip velocity actually exhibits a peak beyond x_c, which sharpens and moves toward x_c as $v \to 0$.[24,30] Thus, we can assume that the tip velocity component perpendicular to the stability boundary is much higher than $\mathbf{v}$. As illustrated in Fig. 1 by the thin blue lines, our numerical simulations indeed show that the direction of tip motion remains essentially unchanged during slips. If $\eta > 1$ the tip trajectory therefore consists of continuous segments (thick blue points) essentially coinciding with the red curve inside stability domains and of straight segments (thin blue lines) during slips between adjacent domains.

The dependence of the *kinetic friction* on the scan angle follows from our earlier discussion of Fig. 2. For symmetry reasons only the range $-45° < \varphi < 45°$ needs to be considered. Due to the absence of cross terms in the equations for F_x and F_y, their long-time average magnitudes are the same and equal to the average in 1D, i.e., $\langle F_x \rangle = |\langle F_y \rangle| = g(\eta)$, where the function $g(\eta)$ has previously been computed assuming slips between adjacent stability domains.[19] It can also be approximated by rather accurate asymptotic expansions for small $\eta - 1$ or $1/\eta$ first derived by Helman *et al.*[31] Thus, the average force acting on the tip apex is always oriented at an angle of $\varphi = 45°$ with respect to the x axis. The kinetic friction measured in FFM is obtained by projecting this force along the scan direction,

$$F_{\text{kin}} = g(\eta)(\cos \varphi + |\sin \varphi|). \tag{9}$$

This expression clearly exhibits a cusp at $\varphi = 0$ and, as shown by the continuous black curve in Fig. 3, agrees well with points obtained from our simulations. Physically the cusp arises because the tip trajectory suddenly flips to the other side of the support path when φ changes sign.

Next we derive expressions for the *static friction*. For $-45° < \varphi < 45°$ the first force jump occurs along the x direction when $x = \arccos(-1/\eta)$. Since the first Eq. (6) is also satisfied, this jump occurs at the critical time t_{cx} such that $x_0 + v_x t_{\text{cx}} = x_{\text{cs}}(\eta)$,

$$x_{\text{cs}}(\eta) = \sqrt{\eta^2 - 1} + \arccos(-1/\eta), \tag{10}$$

being the x coordinate of the support when $x = x_c$. The x component of the elastic force acting on the tip is then $F_{\text{cx}} = \sqrt{\eta^2 - 1}$, as in the 1D case.[32] The corresponding y coordinate of the tip satisfies the second Eq. (6), which becomes

$$F_{\text{cy}} = \eta \sin y_c = y_0 + v_y t_{\text{cx}} - y_c. \tag{11}$$

Substituting the expression for t_{cx} into Eq. (11) one obtains a relation which implicitly defines F_{cy} as a function of the scan angle and the initial offset x_0, y_0. A simple expression is obtained in the limit $\eta \gg 1$: then $x_{\text{cs}}(\eta) \simeq \eta$, so that $F_{\text{cy}} \simeq \eta \tan \varphi$, whereas $F_{\text{cx}} \simeq \eta$. In this limit, Eq. (5) leads to

$$F_{\text{stat}} = \eta \sqrt{1 + \tan^2 \varphi} = \eta / \cos \varphi, \tag{12}$$

independent of the offset. Although Eq. (12) was derived assuming that $\eta \gg 1$, it is in excellent agreement with the values obtained from our simulations performed for $\eta = 5$ if the initial offset is zero. This is shown by the continuous line (red) passing through the squares shown in Fig. 3. However, finite offsets lead to a significant spread of realizable F_{stat} values. The maximum and minimum values as a function of φ derived below are indicated by the triangles pointing up and down, respectively. When $\eta \to \infty$ the two limit curves "coalesce" onto the curve described by Eq. (12). However, the spread shrinks $\sim 1/\eta$, so that the convergence is quite slow. Equation (12) was stated without proof by Wang *et al.*[13] and shown to agree with their numerical simulations for a 2D-FK model in the particular case of zero misfit between two identical square arrays. This is not surprising for two reasons: (i) those simulations were performed by directly applying a force to the top array, (ii) before F_{stat} is reached, the lateral springs connecting the particles trapped in adjacent unit cells are not stretched for zero misfit, so that F_{stat} depends only on E_0 and φ.

Analytic expressions for the limiting values F_{max} and F_{min} of F_{stat} can be derived by substituting the appropriate values F_{cx} and F_{cy} into Eq. (5), which becomes

$$F_{\text{stat}} = \sqrt{\eta^2 - 1} \cos \varphi + \eta \sin y_c \sin \varphi, \tag{13}$$

where according to Eq. (11), y_c satisfies

$$\eta \sin y_c + y_c = y_0 + (x_{\text{cs}} - x_0) \tan \varphi. \tag{14}$$

The scan line being specified by

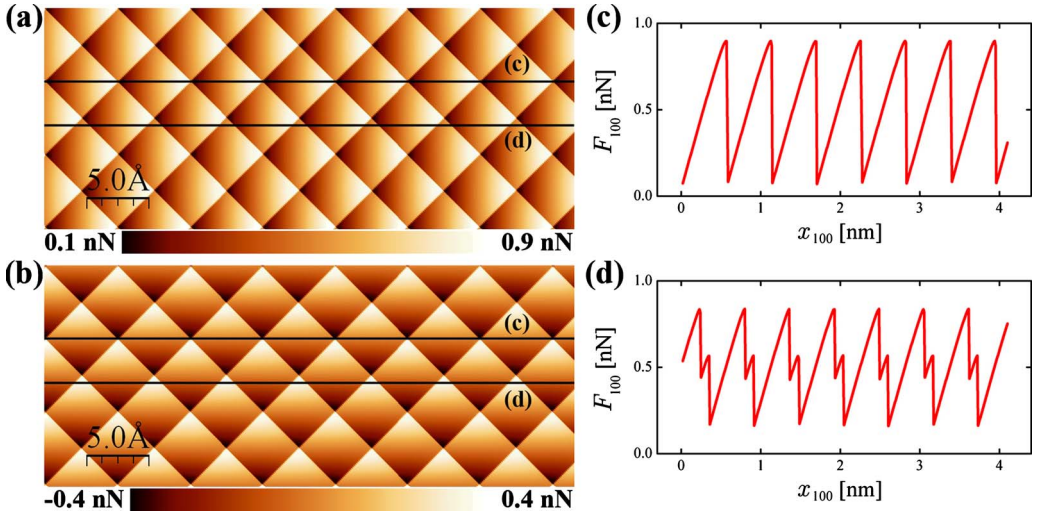

FIG. 4. (Color online) Numerically calculated maps for force components (a) parallel and (b) perpendicular to the [100] scan direction when $\eta=5$. Profiles (c) and (d) are taken along the scan lines marked (c) and (d) in map (a) and show that the subsidiary maximum, which appears in general scan lines like (d), disappears for scan lines like (c) which go over corners of the unit cells.

$$y_s = y_0 + (x_s - x_0)\tan\varphi, \tag{15}$$

x_0 and y_0 can be replaced by suitable values along the scan line in any traversed unit cell, as stated at the end of the preceding section.

When the support crosses the stability boundary at x_{cs}, the force F_{cy} cannot exceed η. This may occur if $y_c=\pi/2$. Since the right-hand side of Eq. (14) increases with y_0 and decreases with x_0, this will happen provided that

$$\tan\varphi > \frac{\eta - \pi/2}{x_{cs} + \pi}. \tag{16}$$

This inequality becomes an equality if in addition $y_0=-x_0=\pi$, i.e., if the scan starts at the left corner of a unit cell in Fig. 1. This occurs when $\varphi=19.26°$ for $\eta=5$, and for $\varphi\to 45°$ if $\eta\to\infty$. If condition (16) is satisfied

$$F_{max} = \sqrt{\eta^2 - 1}\cos\varphi + \eta\sin\varphi, \tag{17}$$

which corresponds to the empty triangles pointing down in Fig. 3. For smaller angles the maximum value of F_{stat} is reached when $y_0=-x_0\to\pi$ and F_{max} is given by Eq. (13) together with Eq. (14) which becomes

$$\eta\sin y_c + y_c = \pi + (x_{cs} + \pi)\tan\varphi. \tag{18}$$

The corresponding F_{max} values are plotted as full triangles pointing down in Fig. 3. On the other hand, the force F_{cy} cannot be less than $-\eta$. This may occur if $y_c=-\pi/2$. By analogy with the preceding discussion, this will happen provided that

$$\tan\varphi < \frac{-\eta + \pi/2}{x_{cs} - \pi}. \tag{19}$$

If condition (19) is satisfied,

$$F_{min} = \sqrt{\eta^2 - 1}\cos\varphi - \eta\sin\varphi. \tag{20}$$

Otherwise, the minimum value is reached when $x_0=-y_0\to\pi$, i.e., if the scan starts at the right corner of a unit cell in Fig. 1. F_{min} is then given by Eq. (13) together with

$$\eta\sin y_c + y_c = -\pi + (x_{cs} - \pi)\tan\varphi. \tag{21}$$

For $\eta=5$, condition (19) cannot be satisfied and the F_{min} values corresponding to Eq. (21) are plotted as full triangles pointing up in Fig. 3.

At first sight it is surprising that F_{max} coincides with the zero offset value of F_{stat} for $\varphi\to\pm 45°$, i.e., for scans along the equivalent ⟨100⟩ and ⟨010⟩ directions. This happens because those directions are singular in several respects. As illustrated in Fig. 4, jumps in the lateral force components (a) parallel and (b) orthogonal to the [100] direction generate maps which reflect the underlying surface lattice. Only the parallel component F_{100} is detected in conventional FFM, and the map in Fig. 4(a) resembles lattice-resolved maps recorded on flat (001) terraces of alkali halides,[18–20] apart from streaks near the cell boundaries attributed to instrumental noise and thermally activated stochastic jumps. The profile of F_{100} along scan line (c) which passes right over minima and maxima of V_{int} shown in Fig. 4(c) exhibits a simple sawtooth pattern with the period of the standard lattice constant $a_1=\sqrt{2}a$. The F_{100} peaks of strength $\sqrt{2}\eta$ are close to F_{max} for $\varphi=\pm 45°$ in Fig. 3, as expected for $\eta=5$, but there is no indication of F_{min}, although the scan line also passes over the left and right corners of the traversed unit cells. However, as first noticed by Hölscher *et al.*[23] on NaF(001), another peak appears in F_{100} [Fig. 4(d)] along all scan lines with a finite offset y_{010} precisely where they cross the cell boundaries on the right. This peak disappears as $y_{010}\to 0$, but becomes as high as first peak when $y_{010}=\pi/2$, i.e., halfway between scan lines passing over minima and maxima, thus producing a sawtooth pattern with period $a_1/2$. The evolution of the F_{100} profile is intimately related to subtle changes in zigzag tip trajectories like that in Fig. 1(c). The "stick times" in the cells centered further form the scan line gradually increase until they become equal to those in the other traversed cells for $y_{010}=\pi/2$.[23,33] If $0<y_{010}<$

$-\pi/2$, the zigzag pattern flips to the other side of the $y_{010}=0$ scan line, and this discrete change is responsible for the finite slope of F_{stat} as $\varphi \rightarrow \pm 45°$ in Fig. 3.

At this juncture it is appropriate to re-examine the measurements of Fujisawa *et al.* in the light of subsequent simulations and insights gained in the meantime. Their data on NaF(001), especially those discussed in their review,[18] are particularly interesting because they were intentionally recorded using normal forces in the nanonewton range in order to realize an atomic-sized contact. At first sight, it seems gratifying that the magnitude of the observed jumps in the measured deflection signals agrees so well with predictions from their simple "stick-point" model. This is, however, a consequence of the calibration procedure (illustrated in Fig. 4 of their review) and of the essentially linear dependence of the measured F_{scan} in the stick stages. In this case, $k_{\text{exp}} \approx k$ in our notation, so that, e.g., for a zero offset scan along [100], the jump in the deflection signal which accompanies a slip to an adjacent unit cell must be close to the change in the same signal induced by a lateral displacement of the support by one lattice constant. The magnitude of F_{100} is, however, seriously overestimated, if one assumes as Fujisawa *et al.*, that k is determined by the lateral stiffness of the cantilever rather than by that of the contact, which is typically smaller at low normal forces. This became apparent only much later.[19]

Additional simulations including thermal fluctuations show that the singularities of zero-offset [100] scans become smeared at RT. Physically this happens because the tip trajectories then consist of noisy stick stages interrupted by x and y slips which occur on *both sides of the scan line* such that the corresponding average proportions gradually change from 1:1 to 1:0 as the offset is increased along [010].

IV. DISCUSSION

The [100]-directed zero-offset scans described above are also of particular interest because the corresponding F_{100} profile versus the support displacement $\mathbf{v}t$ exhibits the strongest variation, i.e., the largest signal-to-noise ratio. They have therefore been used to determine the parameters E_0 and k from the measured maximum value $F_{100}^{\max}$ and from the slope k_{exp} of the stick segments.[19] However, this identification assumed that the 1D-PT model can be applied to analyze such scans.[19] The connection between the 1D and 2D-PT models can be made explicit by expressing the interaction potential in terms of the coordinates $x_1=(x+y)/\sqrt{2}$ and $y_1=(x-y)/\sqrt{2}$ along the [100] and [010] principal symmetry axes. Recalling that $a_1=a\sqrt{2}$, one finds

$$V_{\text{int}} = -E_0 \cos\left(\frac{2\pi x_1}{a_1}\right)\cos\left(\frac{2\pi y_1}{a_1}\right). \tag{22}$$

In previous publications from our group which addressed different aspects of the 2D model,[21,33] the factor in front of Eq. (22) was instead defined as $E_0/2$. In order to avoid confusion this former E_0 is henceforth denoted as $E_{0,\text{old}}$. For the scans in question $y_1=0$ so that

$$V_{\text{int}} = -\frac{E_{0,\text{old}}}{2}\cos\left(\frac{2\pi x_1}{a_1}\right), \tag{23}$$

just as in the 1D model.

Note that because $E_{0,\text{old}}/a_1^2=E_0/a^2$, the parameter η *is the same in both models*. Switching back to real units, in the 1D model[19]

$$F_{100}^{\max} = \pi E_{0,\text{old}}/a_1 = \left(\frac{ka_1}{2\pi}\right)\eta, \tag{24}$$

$$k_{\text{exp}} = \frac{k\eta}{1+\eta}. \tag{25}$$

In the 2D model, Eqs. (5) and (6) imply that for the $\varphi=-45°$ zero offset scan $y=-x$, and

$$F_{100} = \frac{F_x - F_y}{\sqrt{2}} = \frac{k}{\sqrt{2}}\frac{\eta}{1+\eta}2v_x t = \frac{\eta}{1+\eta}kvt \tag{26}$$

for small vt, so that Eq. (25) is satisfied. Moreover, the maximum value of F_{100} is reached when $x=a/4$; therefore

$$F_{100}^{\max} = \sqrt{2}\left(\frac{ka}{2\pi}\right)\eta, \tag{27}$$

which agrees with Eq. (24).

The 1D analysis of [100]-directed zero offset scans is therefore justified, at least if E_0 is sufficiently large compared to $k_B T$.

The temperature-dependent reduction in $\langle F_{100}\rangle$ was computed earlier for $E_{0,\text{old}}=1$, 2, and 4 eV,[21] and found to fit well the $[T\ln(T/v)]^{2/3}$ dependence predicted by the rate theory of ramped creep,[34] except near the superlubric transition. Thus, at RT, $F_{100}^{\max}$ is reduced by factors of 0.50, 0.68, and 0.81 for $E_0=0.5$ eV, 1 eV, and 2 eV, respectively. For the smallest of those values, which corresponds to $\eta=5$, the computed dependence of $\langle F_{100}\rangle$ during stick stages is essentially linear, as shown in Fig. 4(c), so that

$$F_{100}^{\max} \approx \langle F_{100}\rangle + k_{\text{exp}}a_1/2 \tag{28}$$

is essentially subject to the same temperature-dependent reduction as $\langle F_{100}\rangle$. The previously mentioned FFM measurements on NaCl(001) extended up to a *nominal* $E_{0,\text{old}}$ slightly above 0.5 eV [obtained from $F_{100}^{\max}$ by applying Eq. (24) which is valid for $T\rightarrow 0$]. In view of the 50% room-temperature reduction in $\langle F_{100}\rangle$, the *true* $T\rightarrow 0$ values of $E_{0,\text{old}}$ and η should be 1.0 eV and 7.9 ± 1.2 [assuming $k \approx 1.3\pm 0.2$ N/m, according to Fig. 3(d) of Ref. 19].

If $\eta \leq \pi$, deviations from Eq. (28) become significant even for $T\rightarrow 0$. Moreover, according to extensive 1D simulations,[35,36] the temperature-dependent reduction in $\langle F_{100}\rangle$ is stronger in a significantly wider range of $E_0/(k_B T)$ than predicted by the single-spring model adopted here and in Ref. 21. This extended "thermolubricity" arises in two-spring PT models in which the lateral stiffness and dynamics of the cantilever and tip apex are treated separately. In the range in question, the motion of the cantilever is averaged

over rapid thermally activated jumps of the tip apex between two accessible wells of V_{tot} which become equivalent when $x_s = a_1/4$. The intervening energy barrier is then

$$\Delta E \approx \frac{3}{2} E_0 \frac{(\eta - 1)^2}{\eta^2} \tag{29}$$

to lowest order in an expansion about that support position[36] and thus also depends on E_0 via η and gradually increases above the superlubricity threshold. When the contact stiffness is much smaller than the cantilever stiffness, a rather abrupt crossover is predicted between the "thermolubricity" range and the range where the single-spring model and Eq. (28) case become valid.[35] In particular, a further analysis of the room temperature NaCl(001) data[19] showed that thermolubricity extends up to $F_{100}^{\max} \approx 0.25$ nN,[22] i.e., about midway inside the range covered by the data. Above this value, the *true* E_0 and η can be reliably estimated using the computationally much less expensive one-spring model.

In that range, compared to 1D simulations,[34] 2D simulations revealed[21] an additional, nearly constant reduction in $\langle F_{100} \rangle$ by only a factor of 0.9. This is consistent with the effective 1D character of fluctuations which induce thermally activated slips slightly before the tip reaches the boundary of a stability domain. Indeed, according to multidimensional rate theory,[37] such fluctuations preferentially occur along the eigenvector (soft mode) corresponding to the eigenvalue of the Hessian which vanishes at the boundary. The large difference between 1D and 2D simulations claimed in Ref. 24 arises because the authors defined friction as the average of the magnitude $|\mathbf{F}|$ of the lateral force. The common definition in terms of the projection of $\mathbf{F}$ along the scan direction is however, preferable because this component alone contributes to the work done by the support which is ultimately converted into heat if irreversible slips occur.

The ability of the assumed model potential V_{int} to describe angle-dependent FFM measurements on (001) surfaces of cubic crystals, in particular, alkali halides, can be most straightforwardly tested by comparing the measured ratio $\langle F_{100} \rangle / \langle F_{110} \rangle$ of the kinetic friction along the indicated directions with the prediction of Eq. (9), namely, $\sqrt{2}$. Using simulations which included thermal effects,[21] we checked that although both $\langle F_{100} \rangle$ and $\langle F_{110} \rangle$ are significantly reduced at RT, their ratio remains close to $\sqrt{2}$. This observation is consistent with the above-mentioned directional character of thermal fluctuations near stability boundaries. Thus, a comparison of our $T \to 0$ prediction with room-temperature measurements seems justified, at least in the range where the single-spring model applies.

Namai and Shindo[2] found that the ratio measured on five rocksalt-type crystals increases from about 1.4 for KCl to nearly 2.4 for LiF. They also noticed that this trend parallels the increase in the ratio r_-/r_+ of the anion and cation radii which changes from 1.35 for KCl to 2.1 for LiF. Their FFM measurements were performed under ambient conditions at a relatively high load of 23 nN, which likely led to a multiatom contact since the surface lattice could not be imaged. The averages $\langle F_{100} \rangle$ and $\langle F_{110} \rangle$ measured at low relative humidity were, however, constant and thus considered representative. The remarkable agreement between the ratio $\langle F_{100} \rangle / \langle F_{110} \rangle$ predicted by our model potential and the above-mentioned ratio measured on KCl may be fortuitous. Nevertheless the above-mentioned deviation from $\sqrt{2}$ makes physical sense because the curvatures near the saddle points and the minima of V_{int} are expected to increasingly differ for ionic crystals with larger r_-/r_+ ratios. Indeed, in contact measurements on ionic crystals, the modulation of the surface topography at constant normal force, which is simultaneously recorded together with the lateral force F_{scan} in FFM, is mainly determined by the difference between anion and cation radii.

In order to take this difference into account, it is necessary to at least include the next Fourier component of $V_{\mathrm{int}}(x,y)$, namely,[9]

$$-\frac{E_1}{2}\left[\cos\left(\frac{2\pi(x+y)}{a}\right) + \cos\left(\frac{2\pi(x-y)}{a}\right)\right] = -E_1 \cos\left(\frac{2\pi x}{a}\right)\cos\left(\frac{2\pi y}{a}\right). \tag{30}$$

When this expression is added to Eq. (3), and $E_1/E_0 > 0$, the curvature at the minima is higher than at the maxima, which can therefore be associated with the smaller, recessed cations and the larger, protruding anions, respectively. Because the resulting potential is no longer separable, the stability boundaries become curved[9] and an analytic treatment becomes complicated. Leaving a systematic investigation for the future, we note that the present work provides valuable insights into atomic-scale phenomena responsible for the angular dependence of friction forces on a representative class of high-symmetry surfaces, as well as useful benchmark for recognizing deviations from the simple separable 2D-PT model. For instance, E_1 should not only affect the ratio $\langle F_{100} \rangle / \langle F_{110} \rangle$ but also modify the angle and offset dependence of kinetic and static friction. Indeed, a comparison of the tip trajectories in Fig. 1(b) with those in Figs. 1(a) and 1(c) shows that for moderate values of η, scans in off-symmetry directions force the tip to explore the profile of $V_{\mathrm{int}}(x,y)$ further away from minima and saddle points. Comparison with FFM images measured with the same tip in different directions might thus provide independent estimates of E_1 and, possibly, of higher Fourier components of $V_{\mathrm{int}}(x,y)$. The proposed means of characterizing the tip-sample interaction in the contact range is particularly interesting in view of impressive progress in (x,z) or (x,y,z) mapping of the tip-sample interaction in the attractive force range using techniques developed in noncontact atomic force microscopy.[38–41]

V. CONCLUSIONS

In this contribution we derive and validate by numerical simulations simple equations describing the angular dependence of the static and kinetic friction forces acting on a particle pulled by an elastic spring and interacting with a separable model potential with square symmetry. Our simulations provide detailed insights into the atomic-scale origin

of the angular dependence. Comparisons with friction force microscopy measurements show that the model is applicable to (001) surfaces of ionic crystals with comparable cation and anion radii. Furthermore, our work provides a useful framework for identifying deviations in the angle dependence which could reveal atomic-scale details of tip-sample interactions in the contact range. Further extensions, including ordered surfaces with different symmetries and more complex unit cells, anisotropic springs, thermal effects, and larger contact areas are conceivable. Investigations along those lines would certainly improve the understanding of fundamental friction phenomena on the nanoscale.

ACKNOWLEDGMENTS

The Swiss National Science Foundation, the National Center of Competence in Research on Nanoscale Science and the European Science Foundation EUROCORES Programme FANAS are gratefully acknowledged for financial support.

*pascal.steiner@unibas.ch

†Present address: Climate and Environment Physics, University of Bern, Sidlerstr. 5, 3012 Bern, Switzerland.

‡Present address: IMDEA Nanociencia, Campus Universitario de Cantoblanco, Avda. Fco. Tomás y Valiente 7, 28049 Madrid, Spain.

[1] F. P. Bowden and C. A. Brookes, Proc. R. Soc. London, Ser. A **295**, 244 (1966).

[2] Y. Namai and H. Shindo, Jpn. J. Appl. Phys., Part 1 **39**, 4497 (2000).

[3] W. Karino and H. Shindo, Tribol. Int. **40**, 1568 (2007).

[4] Y. Enomoto and D. Tabor, Nature (London) **283**, 51 (1980).

[5] M. Dienwiebel, G. S. Verhoeven, N. Pradeep, J. W. M. Frenken, J. A. Heimberg, and H. W. Zandbergen, Phys. Rev. Lett. **92**, 126101 (2004).

[6] L. Prandtl, Z. Angew. Math. Mech. **8**, 85 (1928).

[7] G. A. Tomlinson, Philos. Mag. **7**, 905 (1929).

[8] O. M. Braun and A. G. Naumovets, Surf. Sci. Rep. **60**, 79 (2006).

[9] T. Gyalog, M. Bammerlin, R. Lüthi, E. Meyer, and H. Thomas, Europhys. Lett. **31**, 269 (1995).

[10] H. Hölscher, U. D. Schwarz, O. Zwörner, and R. Wiesendanger, Z. Phys. B: Condens. Matter **104**, 295 (1997).

[11] T. Gyalog and H. Thomas, Europhys. Lett. **37**, 195 (1997).

[12] G. S. Verhoeven, M. Dienwiebel, and J. W. M. Frenken, Phys. Rev. B **70**, 165418 (2004).

[13] C. Wang, W. Duan, X. Hong, and J. Chen, Appl. Phys. Lett. **93**, 153116 (2008).

[14] M. Dienwiebel, N. Pradeep, G. S. Verhoeven, H. W. Zandbergen, and J. W. M. Frenken, Surf. Sci. **576**, 197 (2005).

[15] J. Colchero, E. Meyer, and O. Marti, in *Handbook of Micro/Nano Tribology*, edited by B. Bhushan (CRC Press, Ohio, 1999).

[16] W. L. Wang, S. J. Hu, and R. Clarke, Phys. Rev. B **68**, 245401 (2003).

[17] S. Fujisawa, Y. Sugawara, S. Ito, S. Mishima, T. Okada, and S. Morita, Nanotechnology **4**, 138 (1993).

[18] S. Morita, S. Fujisawa, and Y. Sugawara, Surf. Sci. Rep. **23**, 1 (1996).

[19] A. Socoliuc, R. Bennewitz, E. Gnecco, and E. Meyer, Phys. Rev. Lett. **92**, 134301 (2004).

[20] S. Maier, Y. Sang, T. Filleter, M. Grant, R. Bennewitz, E. Gnecco, and E. Meyer, Phys. Rev. B **72**, 245418 (2005).

[21] P. Steiner, R. Roth, E. Gnecco, A. Baratoff, S. Maier, T. Glatzel, and E. Meyer, Phys. Rev. B **79**, 045414 (2009).

[22] S. Y. Krylov and J. W. M. Frenken, Phys. Rev. B **80**, 235435 (2009).

[23] H. Hölscher, U. Schwarz, and R. Wiesendanger, Europhys. Lett. **36**, 19 (1996).

[24] C. Fusco and A. Fasolino, Phys. Rev. B **71**, 045413 (2005).

[25] J. Nakamura, S. Wakunami, and A. Natori, Phys. Rev. B **72**, 235415 (2005).

[26] E. Gnecco, S. Maier, and E. Meyer, J. Phys.: Condens. Matter **20**, 354004 (2008).

[27] M. P. Allen and D. J. Tildesley, *Computer Simulation of Liquids* (Clarendon, Oxford, 1990).

[28] H. Hölscher, U. D. Schwarz, O. Zwörner, and R. Wiesendanger, Phys. Rev. B **57**, 2477 (1998).

[29] S. Fujisawa, K. Yokoyama, Y. Sugawara, and S. Morita, Phys. Rev. B **58**, 4909 (1998).

[30] P. Bilas, L. Romana, F. Bade, K. Delbe, and J. L. Mansot, Tribol. Lett. **34**, 41 (2009).

[31] J. S. Helman, W. Baltensperger, and J. A. Holyst, Phys. Rev. B **49**, 3831 (1994).

[32] E. Gnecco, R. Bennewitz, T. Gyalog, and E. Meyer, J. Phys.: Condens. Matter **13**, R619 (2001).

[33] R. Roth, T. Glatzel, P. Steiner, E. Gnecco, A. Baratoff, and E. Meyer, Tribol. Lett. **39**, 63 (2010).

[34] Y. Sang, M. Dube, and M. Grant, Phys. Rev. Lett. **87**, 174301 (2001).

[35] S. Y. Krylov and J. W. M. Frenken, New J. Phys. **9**, 398 (2007).

[36] Z. Tshiprut, A. E. Filippov, and M. Urbakh, J. Phys.: Condens. Matter **20**, 354002 (2008).

[37] G. Vineyard, J. Phys. Chem. Solids **3**, 121 (1957).

[38] A. Schirmeisen, D. Weiner, and H. Fuchs, Phys. Rev. Lett. **97**, 136101 (2006).

[39] K. Ruschmeier, A. Schirmeisen, and R. Hoffmann, Phys. Rev. Lett. **101**, 156102 (2008).

[40] B. J. Albers, T. C. Schwendemann, M. Z. Baykara, N. Pilet, M. Liebmann, E. I. Altman, and U. D. Schwarz, Nat. Nanotechnol. **4**, 307 (2009).

[41] S. Kawai, T. Glatzel, S. Koch, B. Such, A. Baratoff, and E. Meyer, Phys. Rev. B **81**, 085420 (2010).